NANO LETTERS

pubs.acs.org/NanoLett Letter

Thermodynamically Driven Tilt Grain Boundaries of Monolayer Crystals Using Catalytic Liquid Alloys

Min-Yeong Choi,[¶] Chang-Won Choi,[¶] Dong-Yeong Kim, Moon-Ho Jo, Yong-Sung Kim,* Si-Young Choi,* and Cheol-Joo Kim*

Cite This: https://doi.org/10.1021/acs.nanolett.3c00935 Read Online

ACCESS | Metrics & More | Article Recommendations | Supporting Information

ABSTRACT: We report a method to precisely control the atomic defects at grain boundaries (GBs) of monolayer MoS_2 by vapor−liquid−solid (VLS) growth using sodium molybdate liquid alloys, which serve as growth catalysts to guide the formations of the thermodynamically most stable GB structure. The Mo-rich chemical environment of the alloys results in Mo-polar 5|7 defects with a yield exceeding 95%. The photoluminescence (PL) intensity of VLS-grown polycrystalline MoS_2 films markedly exceeds that of the films, exhibiting abundant S 5|7 defects, which are kinetically driven by vapor−solid−solid growths. Density functional theory calculations indicate that the enhanced PL intensity is due to the suppression of nonradiative recombination of charged excitons with donor-type defects of adsorbed Na elements on S 5|7 defects. Catalytic liquid alloys can aid in determining a type of atomic defect even in various polycrystalline 2D films, which accordingly provides a technical clue to engineer their properties.

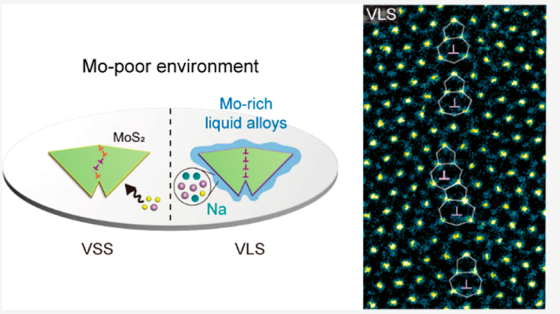

KEYWORDS: *two-dimensional materials, grain boundary, atomic defect, catalytic alloy, vapor−liquid−solid growth, doping*

Structural defects in a polycrystalline two-dimensional (2D) structure can often re-form the material properties beyond those of single crystals.[1] In particular, grain boundaries (GBs) contain various atomic defects that exhibit novel electrical,[2,3] magnetic,[4,5] mechanical,[6,7] and chemical[8−10] properties. The emergent properties of GBs are extremely sensitive to atomic arrangements with short-range ordering, which are thermodynamically metastable and thus can have variable configurations. To obtain desirable properties associated with specific structural defects, GB structures must be elaborated upon at the atomic level. Yet, polycrystalline 2D structures have exhibited uncontrolled GBs in which various defect structures coexist.[11,12]

The structures of tilt GBs are primarily characterized by two structural parameters: the tilt angle, θ_t, and the inclination angle, Φ, of defects within the lattice (Figure 1a). In transition-metal dichalcogenides (MX_2; M = transition metal, X = chalcogen) such as MoS_2 with 3-fold rotational symmetry, the magnitude of θ_t varies from 0 to 60°, and the defect density increases as θ_t increases (see Figure S1 for atomic configurations as a function of θ_t). While it is energetically favorable to form pentagon−heptagon (5|7) defects with the smallest Burgers vector, $\vec{b}$, considering the strain energy of GBs,[13] the 5|7 defects have a structural degree of freedom to exhibit two types of homoelemental bonding (HB), either M−M or X−X, depending on Φ, which is associated with the crystallographic orientation of defects.[11,14] Here, we define Φ by the relative rotational angle between the defect direction vector, $\vec{x}$ (dotted blue arrow) and the symmetric GB vector, $\vec{v}$ (solid black arrow), where $\vec{x}$ is parallel to the vertical mirror plane of the defects, pointing to the seven-ring from the five-ring, and $\vec{v}$ is aligned to the symmetric armchair (AC) direction between the two tilted zigzag (ZZ) axes (dotted lines) of the merged grains. The defects with Φ = 0° form 5|7-membered rings with Mo−Mo HB (Mo 5|7), whose $\vec{b}$ is equal to $\vec{a}_1$. On the other hand, the defects with Φ = 60° result in S 5|7 structures with S−S HB that have $\vec{b}$ of $\vec{a}_2$. In theory, the formation of specific defects can be thermodynamically guided by modulating the chemical potential of the environment.[15] While the Mo 5|7 defect is more stable than the S 5|7 defect in a Mo-rich environment with low S chemical potential, μ_s, the S 5|7 defect becomes more stable than the Mo 5|7 defect in a Mo-poor environment with high μ_s (Figure 1b).

Although individual control of M- and X-containing precursors during vapor-phase growth[16,17] would be the simplest way of changing μ_s to determine the thermodynamically most stable defect structures, two main factors prevent

Received: March 11, 2023
Revised: May 6, 2023

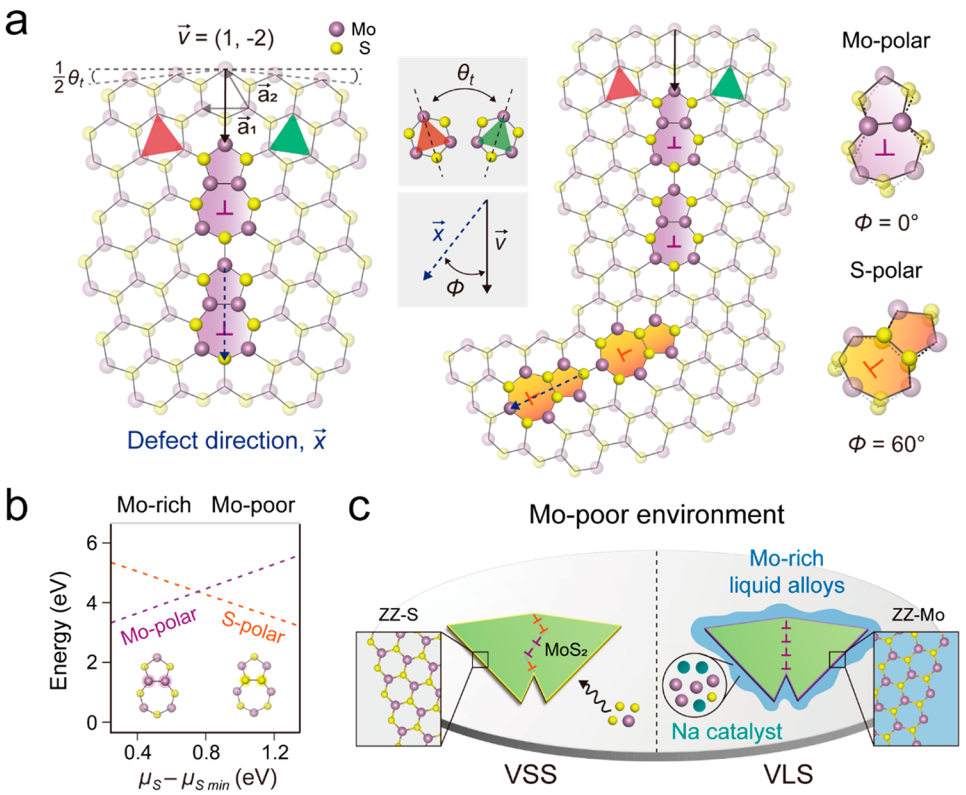

Figure 1. Growth-mode-dependent GBs. (a) Schematics of the formation of tilt boundaries. Stitching of grains tilted by θ_t can form Mo 5|7 defects with Φ = 0° and S 5|7 defects with Φ = 60°. (b) Density functional theory (DFT) calculations for the formation energy of GB defects with Mo−Mo or S−S HB as a function of $\mu_s - \mu_{s\,min}$ of the growth environment (see the Supporting Information for the definition of $\mu_{s\,min}$). (c) Illustration of VSS and VLS growth modes with different chemical environments, which result in a kinetically driven mixture of Mo 5|7 and S 5|7 defects and a thermodynamically driven array of homogeneous Mo 5|7 defects, respectively.

this approach from realizing the deterministic formation of specific atomic defects. First, owing to the spatiotemporal fluctuations of introduced gaseous precursors, developing uniform environments across a large area is challenging. If a large amount of either M or X elements is supplied to induce an extreme chemical environment for selective defect formations that resist the fluctuation of vapor flows, the excess elements can produce undesired byproducts, such as solid M or X and other compounds.[18,19] Second, the final GB structures are often set kinetically. When the continuous growth of adjacent grains tilted by a specific θ_t "zips-up" the gap between joint grains, the geometric boundary condition can limit possible Φ, resulting in thermodynamically unfavorable defect structures under the given chemical condition[20,21] (see Figure S2 for the schematics of the process). To laterally connect tilted grains with defects of the same Φ, GB migration by reordering atomic structures is required to overcome a significant energy barrier.[22] Notably, in previous studies, even growth with a controlled chemical environment resulted in polycrystalline MoS_2, where two types of different GBs with orientations tilted by roughly 60° coexisted at the joint of merged grains,[20,23] suggesting the kinetically driven formation of GBs.[21]

We propose a synthetic strategy to utilize catalytic alloys of sodium molybdate, Na−Mo−O, in metal−organic chemical vapor deposition (MOCVD).[16] The eutectic composition[24] of a high Mo concentration of about 20 mol % can provide a stable, low-μ_s environment with a large amount of chemically active Mo elements in a liquid phase,[25] via which vapor−liquid−solid (VLS) growth occurs. In addition, the Na element in the liquid alloys functions as a catalyst to lower the energy barrier for the transformation of the other kinetically driven defect structures to Mo 5|7 defects.[26] This approach is possible due to the 2D structure of the material, where all the GBs are exposed on the surface to interact with the catalytic alloys.

Monolayer MoS_2 was grown with and without liquid alloys in a single batch to test their roles in GB defect formation (Figure 1c; detailed methods are given in the Supporting Information).[27] The GBs of the two polycrystalline MoS_2 films grown by vapor−solid−solid (VSS) and VLS growth, respectively, were directly visualized using a scanning transmission electron microscope with a high-angle annular dark field detector (HAADF-STEM). Tilted grains of θ_t formed by VSS and VLS growths are shown in the inverse fast Fourier transform (FFT) images of the STEM image data by selecting reciprocal points, where the ZZ planes of each grain are color-coded differently (Figure 2a,b). Notably, the GB was nearly aligned to the symmetric axis of $\vec{v}$ in the VLS growth, whereas it was rotated roughly by 30° with respect to $\vec{v}$ in the VSS growth. In the HAADF-STEM data at the atomic scale (Figure 2c,d), defects with two different Φ, close to either 0° (highlighted with purple ⊥) or 60° (red ⊥) coexisted in the VSS growth. However, although the entire GB was still asymmetric, forming a nonstraight line, $\vec{x}$ of all defects was closely parallel to $\vec{v}$ with $\Phi \approx 0°$ in the VLS growth (see Figures S3 and S4 for STEM data over different GB areas). The statistics for Φ values and atomic structures of defects are shown for both VSS and VLS growths from 150 defects in total (Figure 2e). VLS growth resulted in Mo 5|7 defects with a

https://doi.org/10.1021/acs.nanolett.3c00935
Nano Lett. XXXX, XXX, XXX−XXX

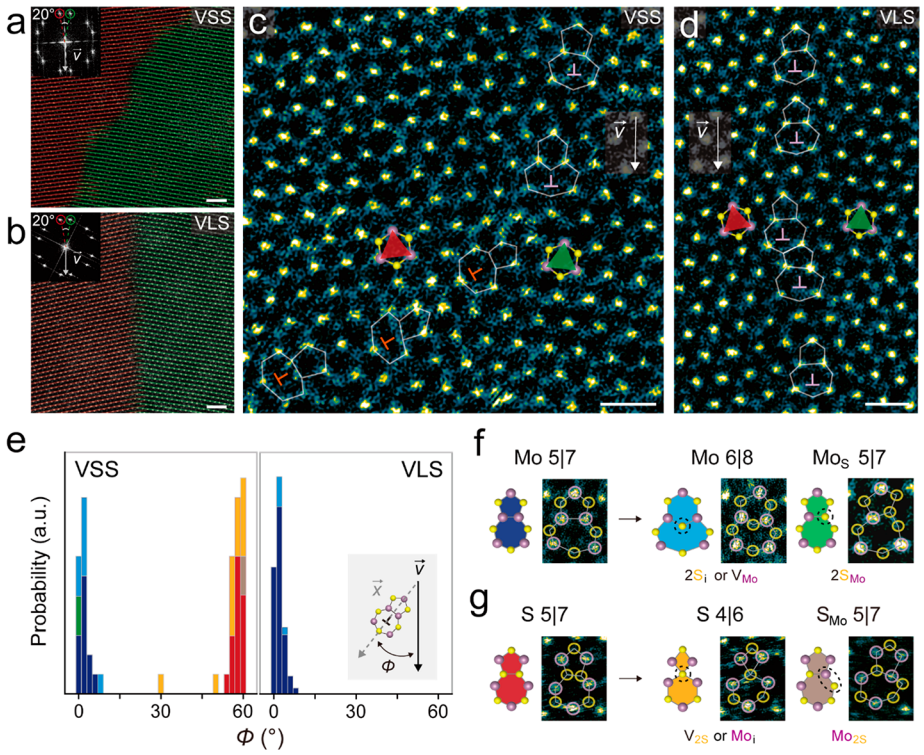

Figure 2. Comparison of GB structures between VSS and VLS growth modes. (a, b) FFT filtered STEM images of GB structures with a θ_t of 20° formed by (a) VSS mode and (b) VLS mode. (Inset) Diffraction pattern images show two spots (red and green circles) with a 20° rotation and $\vec{v}$ aligned to the symmetric direction of the two merged crystalline grains. Scale bar: 1 nm. (c, d) Magnified atomic images of each GB structure in (a) and (b). Scale bar: 0.5 nm. (e) Statistics of Φ and the types of atomic structures for defects at tilt GBs formed by each growth mode. Here, the Φ values are defined between 0 and 60°, considering the 3-fold rotational symmetry (Φ = Φ + 120°) and the in-plane mirror symmetry (Φ = − Φ) of the MoS_2 crystal. (f, g) Atomic reconstruction processes of (f) Mo 5|7 and (g) S 5|7 defects to their derivatives. Mo 5|7 derivatives occur at relatively high μ_s, resulting in Mo 6|8 by S interstitials or Mo vacancies and Mo$_S$ 5|7 by 2S substitution for the Mo sites of HB. S 5|7 derivatives include S 4|6 by double S vacancies or Mo interstitials, formed in relatively low μ_s and S$_{Mo}$ 5|7 with a Mo switched positions with S atoms.

yield >95% along the GBs, with the defects exclusively pointing to Φ ≈ 0°. However, VSS growth resulted in varying defects.

Changes in the defect structures by incorporating interstitial or substitutional elements (Figure 2f,g) can happen easily, while maintaining the Φ due to the low activation energies.[15] Because the local chemical environment can vary over time during VSS growth, the atomic defects can translate into the new structure, resulting in various derivatives for both Mo 5|7 and S 5|7 defects.[14] The formation of Mo 5|7 and S 5|7 defects were expected to occur in completely different regimes of μ_s (Figure 1b), implying that their coexistence indicates a large temporal variation in local chemistry during vapor-phase growth. However, during VLS growth, Mo 5|7 defects formed at the low μ_s were preserved by the nearby liquid alloys after stitching of grains. Because the alloys comprise more Mo and S elements than in gaseous environments, the chemical potential within the alloys can be mostly maintained despite temporal vapor pressure fluctuations.[25]

Meanwhile, simply modulating the growth environment without a catalytic reaction would kinetically limit GB structures, resulting in both 0 and 60° for the Φ values.[11] If the energy barrier for the growth kinetics of kink nucleation and propagation is high,[21] the rough GBs, even at the nanometer scale, can be formed with multiple kinks and various defects of different Φ values. However, in our VLS growth, although merging two adjacent edges of tilted grains with Mo 5|7 defects was geometrically restricted at local areas, MoS_2 near the GBs could be continuously dissolved in the liquid alloys and then resolidified, prompting the reordering of the crystalline structures with Na catalysts[26] to form the thermodynamically most stable Mo 5|7 defect with Φ ≈ 0°. Indeed, we observed smooth GBs without noticeable kinks in VLS growth, which are thermodynamically expected forms with minimized total lengths of GBs between two tilted grains to lower the structure's total energy.[28]

Now, we discuss how the GB structures change as a function of θ_t. We deduce the density of defects, $d_{defects}$, along GBs of different θ_t by the inverse value of the averaged distances between defects with the same Φ. In both samples grown by VLS and VSS modes, $d_{defects}$ increased monotonically as θ_t increased in a quantitatively similar manner (Figure S5). The change in θ_t was closely matched with the model for the maximum relaxation of strains at the tilt GB by formations of defects (see the Supporting Information for the tilt-boundary model).[29] At GBs with $\theta_t \approx 34°$, $d_{defects}$ became large enough to form closely packed defects with Φ ≈ 0° in series (Figure S3). Because accommodating a larger $d_{defects}$ with a single type of defect at a tilt GB with $\theta_t > 34°$ is difficult, theories predict the formation of alternating Mo 5|7 and S 5|7 defects, pointing to different orientations for relaxing the local strains at the GBs.[4,6] Therefore, when stitching grains with a single type of defect structure in polycrystalline films, high-θ_t GB formation must be avoided. The MoS_2 grains are grown on amorphous surfaces; therefore, their crystallographic orientations should be randomly defined, meaning that θ_t values between merging grains can have any value up to 60°, including high θ_t.

https://doi.org/10.1021/acs.nanolett.3c00935
Nano Lett. XXXX, XXX, XXX−XXX

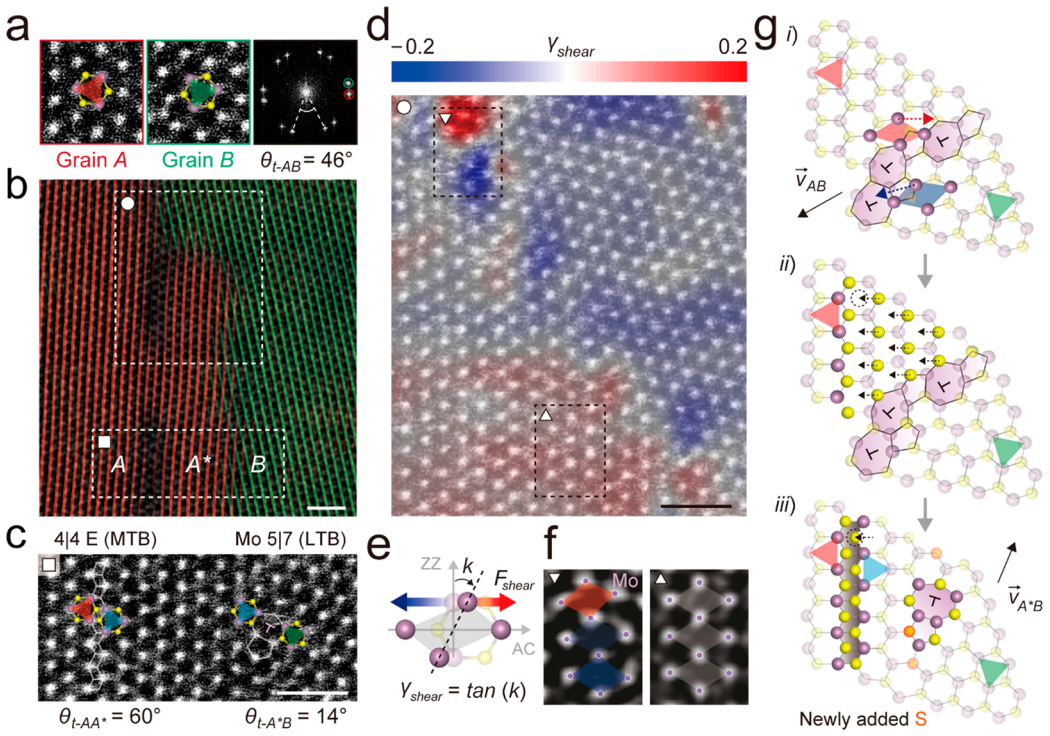

Figure 3. Deformation−twinning process at high θ_t stitching. (a) STEM images and corresponding FFT pattern of closely located A and B grains, in which the in-plane crystallographic orientations are rotated by 46°. (b) Combined atomic image and false-color FFT-filtered image. The FFT image was obtained by selecting two spots (red and green circle) of the diffraction pattern in (a). Scale bar: 1 nm. (c) Enlarged image over the dotted area in (b) (□), showing three (*A*, *A**, *B*) regions with different crystallographic orientations. $\theta_{t\text{-}AA^*}$ is the tilt angle between *A* and *A** regions; $\theta_{t\text{-}A^*B}$ is the tilt angle between *A** and *B* regions. Scale bar: 1 nm. (d) The γ_{shear} map, combined with the atomic image at the dotted area in (b) (○). Scale bar: 1 nm. (e) A schematic to describe shear strain, γ_{shear}, from the distorted MoS_2 unit cell. Shear force applied toward the AC direction generates the distortion angle, *k*. γ_{shear} is defined as the tangent value of *k*. (f) Enlarged STEM images of the high-strained (▽) and low-strained regions (△) from (d). The local structural distortions are presented by different colors, as described in (e). (g) Schematics for the deformation−twinning process to generate the GB structure in (a−f).

Nevertheless, we did not observe high-θ_t GBs with θ_t > 34°, indicating a self-exclusion of the formations of high-θ_t GBs.

We investigated the regions near two grains with a high misorientation angle of 46°. An atomic STEM image is overlaid with its false-color inverse FFT image, which presents the ZZ planes of two tilted grains, corresponding to reciprocal points from each grain (Figure 3a,b). We found that if a certain reciprocal point was selected for the inverse FFT from the *A* grain, the resultant image showed a reduced intensity along the linear region within the grain, separating the grain into *A* and *A** grains. The reduced intensity indicated a missing ZZ plane corresponding to the selected reciprocal point. In the atomic image (Figure 3c) across the boundary regions (□ region in Figure 3b), we found that the inverse *A* and *A** grains are translated slightly along the ZZ direction to form a mirror-twin boundary (MTB) with a one-dimensional chain of edge-shared 4|4 defects (4|4 E), and a low tilt angle, $\theta_{t\text{-}A^*B}$, was formed between the *A** grain and *B* grain. The tilt angle between the *A* grain and *B* grain $\theta_{t\text{-}AB}$ of 46° was equivalent to the sum of $\theta_{t\text{-}AA^*}$ and $\theta_{t\text{-}A^*B}$. The $\theta_{t\text{-}AA^*}$ for MTB was 60° or equivalent to 180°, considering the 3-fold rotational symmetry, and $\theta_{t\text{-}A^*B}$ was −14°; the negative sign means that the tilt angle polarity for $\theta_{t\text{-}A^*B}$ is opposite to that of $\theta_{t\text{-}AA^*}$. Meanwhile, the defects at the GB between the *A** grain and *B* grain form Mo 5|7 defects. GB-mediated deformation twinning in other regions is also presented in Figure S6.

To understand the deformation−twinning process, we present a shear strain, γ_{shear}, map in Figure 3d (○ region in Figure 3b). γ_{shear} is deduced by tan *k*, where *k* indicates the local distortion angle of the ZZ axis toward the clockwise direction with respect to the perpendicular direction of the AC axis from the image of Mo atoms (Figure 3e). High local strains of $|\gamma_{shear}| \approx 0.2$ with opposite polarities are present near the intersection between MTB and low-θ_t GB, where two grains with high θ_t are directly connected. In contrast, the strains show small values of <0.03 in other regions, including the areas near MTB and low-θ_t GB, indicating that the deformation twinning can effectively relax the strain at high-θ_t GBs (see Figure 3f for the atomic images of the high-strained and low-strained regions, which are highlighted in Figure 3d).

Our hypothesis for the deformation−twinning process that formed the structure in Figure 3d is illustrated in Figure 3g. When tilted A and B grains with a high $\theta_{t\text{-}AB}$ were merged, closely packed single-type defects were formed to stitch the two grains (Figure 3g, step *i*). Due to the low-μ_s environment, given by the liquid alloys, Mo 5|7 defects inclined to $\vec{v}_{AB}$ with $\Phi \approx 0°$ were selectively formed. Because d_{defect} for the single type of Mo 5|7 defect was limited, high residual strains were accumulated near the GB with Mo HBs, which were the weakest bonds in the lattice (see Figure S7 and discussion for the structural analyses of defects in the Supporting Information). A γ_{shear} above the critical value causes structural instability. As discussed earlier, forming additional S 5|7 defects provides a way to release the strain; however, S 5|7 defects are thermodynamically unfavorable at low μ_s. Another possible structural transformation to release the strain is the lateral

https://doi.org/10.1021/acs.nanolett.3c00935
Nano Lett. XXXX, XXX, XXX−XXX

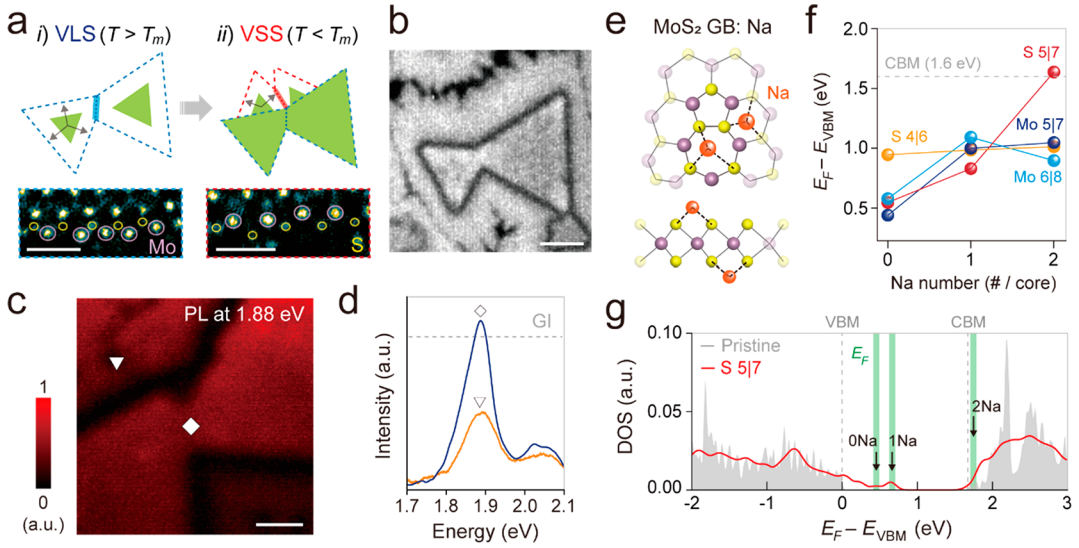

Figure 4. PL properties of VLS- and VSS-grown GBs. (a) Consecutive VLS and VSS growth for direct comparison of each GB with a similar θ_t. Inset: STEM atomic images for edges grown by each growth mode. Scale bar: 0.5 nm. (b) PL intensity mapping image for the resultant sample grown by the method shown in (a). Scale bar: 5 μm. (c) PL intensity mapping image for VLS- and VSS-GBs with an excitation energy of 1.88 eV and incident power density of ~ 5 × 10^3 W/cm^2. Scale bar: 1 μm. (d) PL spectra corresponding to (c). The dotted lines indicate the intensities measured at the grain interiors. (e) Schematics of top- and side-view atomic structures of Na adsorbed at a defect of MoS_2 GBs. (f) Change of the E_F for the structure in (e) with respect to the valence band maxima (VBM) of the pristine lattice as a function of the number of Na atoms adsorbed on different GB defects. (g) Electronic structure of S 5|7 defects embedded in monolayer MoS_2. The gray plot indicates the density of state (DOS) for pristine MoS_2 without defects, and the red plot indicates DOS for the defects. The gray dotted lines show VBM and the conduction band minima (CBM) for the pristine lattice. The highlighted green lines indicate the levels to be occupied by the electrons from Na atoms. As the adsorbed Na atoms increase, the occupation levels also increase.

gliding of the S planes in one of the grains (step *ii*). If the gliding of S planes is pinned to a certain point (step *iii*), an MTB with 4|4 E defects (highlighted in gray) is formed.[30] The deformation−twinning process relaxes the total interfacial and strain energy. MTB lacks energetically unfavorable HB in terms of chemical energy. The emerging low-tilted boundary (LTB) has an HB, but its $d_{defects}$ is significantly lower than that of the high-tilt GB. Therefore, when an MTB nucleates by a critical strain field at an unstable tilted GB, it can spontaneously grow by inducing cooperative displacement of S atoms, resulting in twinning with plastic deformation. After the process, the strain field only remains at the intersection between coherent MTB and incoherent, curved LTB.[31] Notably, the absorption and emission of defects during the deformation−twinning process in VLS growth selectively left Mo 5|7 defects as a stable GB structure.

To identify the roles of different defects in determining the physical properties of polycrystalline materials, we further compared the photoluminescence (PL) near the GBs formed by VLS and VSS growths (Figure 4). For a direct comparison, we devised a growth method by which VLS- and VSS-GBs with a similar θ_t can be simultaneously generated in a single sample. Here, the growth mode was switched from the VLS mode to the VSS mode on SL substrates by lowering the temperature during the growth below the melting point of Na−Mo−O alloys, T_m ≈ 500 °C (Figure 4a). In STEM images, we confirmed that the edges of the first-grown region (Figure 4a, blue dotted line and box) and the second-grown region (red dotted line and box) of the single crystal showed ZZ−Mo and ZZ−S edges, respectively, which were expected for low and high μ_s for each growth mode[32] (see Figure S8 and the Supporting Information for the experimental details). By the two-step growth, tilted grains could be stitched by either VLS or VSS growths, generating VLS (Figure 4a, highlighted by solid blue line)- and VSS-GBs (solid red line), respectively.

The VLS- and VSS-grown regions were clearly distinguished in the PL intensity mapping images of the as-grown samples (Figure 4b), where the PL intensity near the triangular boundaries between the VLS- and VSS-grown regions was significantly quenched by the solidified alloys along the boundaries. We observed that the PL spectra from the grain interior (GI) showed similar intensities in both VLS- and VSS-grown regions, suggesting that the growth mode did not affect the GI's atomic structures. Considering the relative angle between the lines with quenched PL in the merged grains, we deduced θ_t. Representative PL mapping data (Figure 4c) near the tilt, VLS- and VSS-GBs of θ_t ≈ 33°, showed different behaviors. The PL intensity at the VLS-GB (the region indicated by the ◇ symbol in Figure 4c) was similar to that from the nearby GI. In contrast, at VSS-grown GBs (the region indicated by the ▽ symbol in Figure 4c), the PL peak was red-shifted by ~10 meV with significant suppression of intensities by as much as ~55% at an incident power density of ~5 × 10^3 W/cm^2 (Figure 4d). In the measurements on different samples, VLS-GBs always showed PL intensity similar to or even higher than that of GIs, whereas VSS-GBs often showed lower intensities than GIs. We also measured the global PL over 30 × 30 μm^2 are in the continuous films with polycrystalline structures, which we synthesized by VLS and VSS growth modes, separately. The PL spectra showed significantly stronger intensities in the VLS-grown films than in the VSS-grown films (Figure S9). By spectral deconvolution, the negative trion peak area I_{tr} and exciton peak area I_{ex} were deduced, and the ratio of the spectral weights w was calculated as I_{tr}/I_{ex} = 0.28 for VLS-grown films and 0.46 for VSS-grown films (Figure S9). The result suggests the spontaneous

https://doi.org/10.1021/acs.nanolett.3c00935
Nano Lett. XXXX, XXX, XXX−XXX

formation of negative trions with the existence of the electron doping concentration, n, which have a lower efficiency for radiative recombination than do excitons.[33,34]

We conducted DFT calculations to understand how the main four defects observed in our samples (i.e., Mo 5|7, Mo 6|8, S 5|7, and S 4|6 defects) changed n. The calculations show that all the calculated defects form deep-level defect states near midgap, which cannot contribute to an effective electron doping at room temperature (Figure S10). Then, we speculated that the defects host other donor-like impurities. According to our calculations, Na atoms interact more strongly with the Mo 5|7, Mo 6|8, S 5|7, and S 4|6 defects than with the pristine lattice, presumably due to their strong tendency to capture electrons from the alkali metal. All the defect structures can spontaneously host two Na atoms, as depicted in the schematics of Figure 4e. We calculated E_F for GB loop structures with atomic defects and different numbers of Na elements (Figure S11) and compare the level with E_F for the pristine lattice (Figure 4f) to estimate the efficiency of the adsorbed Na atoms for doping of free electrons to the MoS_2 lattice. With Mo 5|7, Mo 6|8, and S 4|6 defects, E_F values are located at a deep level below the conduction band edge of the pristine lattice by ∼1 eV with two surrounding Na atoms. However, for S 5|7 defects, the position of E_F moves within the conduction band (Figure 4g). The electron trap efficiency of the atomic defects is related to the density of trap states of the defects. S 5|7 defects have fewer midgap states to trap free electrons than other Mo 5|7, Mo 6|8, and S 4|6 defects. Therefore, S 5|7 defects cannot fully accommodate the electrons, donated by Na atoms, keeping the free electrons from Na atoms in the MoS_2 lattice, while other defects effectively trap all the electrons. We note that the defects could host other impurities to change the electron doping level as well,[35] but we suspect that the electron trap efficiency would be still higher nearby Mo 5|7, Mo 6|8, and S 4|6 defects for the same reason mentioned above. We have further conducted quantitative comparisons between n values, deduced from the theory and the experimentally measured PL, and they showed reasonable agreements (Supporting Information).

In conclusion, we demonstrated that using catalytic liquid alloys can provide a powerful approach with unprecedented precision for defect control at GBs by thermodynamics. We showed that the electrical doping level of the 2D films significantly depends on the type of defects at GBs due to their different interactions with foreign elements. Our technique can be broadly applied to engineer various electrical, chemical, and mechanical properties of 2D materials, realizing novel structures such as one-dimensional quantum wires,[3] single-atom catalysts,[36] and extremely flexible membranes.[37] Finally, if appropriate alloys can be developed, this approach is versatile enough to produce various atomic defects in a library of 2D materials.

■ ASSOCIATED CONTENT

Supporting Information

The Supporting Information is available free of charge at https://pubs.acs.org/doi/10.1021/acs.nanolett.3c00935.

Experimental details for MoS_2 growth and STEM characterizations, tilt-boundary model, shear strain analyses, details for DFT calculations, PL analysis model, structural analyses of defects, schematics for atomic configurations of tilt-GBs, schematics for GB formation processes, STEM atomic images of VLS- and VSS-GBs, $d_{defects}$ as a function of θ_t, STEM image of double GBs, structural analyses of Mo 5|7 and S 5|7 defects, two-step growth data, PL measurements in polycrystalline MoS_2 films, electronic band structures for MoS_2 with defects, and Fermi level change by the Na-adsorbed GB defects (PDF)

■ AUTHOR INFORMATION

Corresponding Authors

Yong-Sung Kim − *Korea Research Institute of Standards and Science, Daejeon 34113, Republic of Korea; Department of Nano Science, University of Science and Technology, Daejeon 34113, Republic of Korea;* orcid.org/0000-0002-6057-2997; Email: yongsung.kim@kriss.re.kr

Si-Young Choi − *Center for Van der Waals Quantum Solids, Institute for Basic Science (IBS), Pohang 37673, Republic of Korea; Department of Materials Science & Engineering and Department of Semiconductor Engineering, POSTECH, Pohang 37673, Republic of Korea;* orcid.org/0000-0003-1648-142X; Email: youngchoi@postech.ac.kr

Cheol-Joo Kim − *Center for Van der Waals Quantum Solids, Institute for Basic Science (IBS), Pohang 37673, Republic of Korea; Department of Chemical Engineering, Pohang University of Science and Technology (POSTECH), Pohang 37673, Republic of Korea;* orcid.org/0000-0002-4312-3866; Email: kimcj@postech.ac.kr

Authors

Min-Yeong Choi − *Center for Van der Waals Quantum Solids, Institute for Basic Science (IBS), Pohang 37673, Republic of Korea; Department of Chemical Engineering, Pohang University of Science and Technology (POSTECH), Pohang 37673, Republic of Korea;* orcid.org/0000-0001-6966-3513

Chang-Won Choi − *Center for Van der Waals Quantum Solids, Institute for Basic Science (IBS), Pohang 37673, Republic of Korea; Department of Materials Science & Engineering, POSTECH, Pohang 37673, Republic of Korea;* orcid.org/0000-0003-3620-7460

Dong-Yeong Kim − *Center for Van der Waals Quantum Solids, Institute for Basic Science (IBS), Pohang 37673, Republic of Korea; Department of Chemical Engineering, Pohang University of Science and Technology (POSTECH), Pohang 37673, Republic of Korea*

Moon-Ho Jo − *Center for Van der Waals Quantum Solids, Institute for Basic Science (IBS), Pohang 37673, Republic of Korea; Department of Materials Science & Engineering, POSTECH, Pohang 37673, Republic of Korea;* orcid.org/0000-0002-3160-358X

Complete contact information is available at: https://pubs.acs.org/10.1021/acs.nanolett.3c00935

Author Contributions

¶M.-Y.C. and C.-W.C. contributed equally to this work. S.-Y.C. and C.-J.K. designed the experiments. M.-Y.C. grew MoS_2 samples. M.-Y.C. and D.-Y.K. conducted PL measurements. C.-W.C. and S.-Y.C. performed the (S)TEM imaging and analysis. Y.-S.K. performed the DFT calculations. All authors contributed to the data analysis. M.-Y.C. and C.-J.K. wrote the manuscript with inputs from all authors.

https://doi.org/10.1021/acs.nanolett.3c00935
Nano Lett. XXXX, XXX, XXX−XXX

Notes

The authors declare no competing financial interest.

■ ACKNOWLEDGMENTS

This research was supported by the National R&D Program through the National Research Foundation of Korea (NRF) funded by the Ministry of Science and ICT (2023R1A2C2005427, 2020M3D1A1110548, 2022M3H4A1A01012718), the Institute for Basic Science (IBS-R034-D1), and Samsung Electronics Co., Ltd. The microscopic experiments and analyses were supported by a Korea Basic Science Institute (National Research Facilities and Equipment Center) grant funded by the Ministry of Education (2020R1A6C101A202).

■ REFERENCES

(1) Yang, S.-J.; Choi, M.-Y.; Kim, C.-J. Engineering grain boundaries in two-dimensional electronic materials. *Adv. Mater.* **2023**, *35*, 2203425.
(2) Ly, T. H.; Perello, D. J.; Zhao, J.; Deng, Q.; Kim, H.; Han, G. H.; Chae, S. H.; Jeong, H. Y.; Lee, Y. H. Misorientation-angle-dependent electrical transport across molybdenum disulfide grain boundaries. *Nat. Commun.* **2016**, *7*, 10426.
(3) Jolie, W.; Murray, C.; Weiß, P. S.; Hall, J.; Portner, F.; Atodiresei, N.; Krasheninnikov, A. V.; Busse, C.; Komsa, H. P.; Rosch, A.; Michely, T. Tomonaga-Luttinger liquid in a box: electrons confined within MoS_2 mirror-twin boundaries. *Phys. Rev. X* **2019**, *9*, 11055.
(4) Zhang, Z.; Zou, X.; Crespi, V. H.; Yakobson, B. I. Intrinsic magnetism of grain boundaries in two-dimensional metal dichalcogenides. *ACS Nano* **2013**, *7*, 10475−10481.
(5) Gao, N.; Guo, Y.; Zhou, S.; Bai, Y.; Zhao, J. Structures and magnetic properties of MoS_2 grain boundaries with antisite defects. *J. Phys. Chem. C* **2017**, *121*, 12261−12269.
(6) Yang, L.; Liu, J.; Lin, Y.; Xu, K.; Cao, X.; Zhang, Z.; Wu, J. Strengthening and weakening by dislocations in monolayer MoS_2. *Chem. Mater.* **2021**, *33*, 8758−8767.
(7) Wu, J.; Gong, H.; Zhang, Z.; He, J.; Ariza, P.; Ortiz, M.; Zhang, Z. Topology and polarity of dislocation cores dictate the mechanical strength of monolayer MoS_2. *Appl. Mater. Today* **2019**, *15*, 34−42.
(8) Zhu, J.; Wang, Z. C.; Dai, H.; Wang, Q.; Yang, R.; Yu, H.; Liao, M.; Zhang, J.; Chen, W.; Wei, Z.; Li, N.; Du, L.; Shi, D.; Wang, W.; Zhang, L.; Jiang, Y.; Zhang, G. Boundary activated hydrogen evolution reaction on monolayer MoS_2. *Nat. Commun.* **2019**, *10*, 1348.
(9) Liu, L.; Ye, K.; Lin, C.; Jia, Z.; Xue, T.; Nie, A.; Cheng, Y.; Xiang, J.; Mu, C.; Wang, B.; Wen, F.; Zhai, K.; Zhao, Z.; Gong, Y.; Liu, Z.; Tian, Y. Grain-boundary-rich polycrystalline monolayer WS_2 film for attomolar-level Hg^{2+} sensors. *Nat. Commun.* **2021**, *12*, 3870.
(10) Karvonen, L.; Säynätjoki, A.; Huttunen, M. J.; Autere, A.; Amirsolaimani, B.; Li, S.; Norwood, R. A.; Peyghambarian, N.; Lipsanen, H.; Eda, G.; Kieu, K.; Sun, Z. Rapid visualization of grain boundaries in monolayer MoS_2 by multiphoton microscopy. *Nat. Commun.* **2017**, *8*, 15714.
(11) van der Zande, A. M.; Huang, P. Y.; Chenet, D. A.; Berkelbach, T. C.; You, Y.; Lee, G.-H.; Heinz, T. F.; Reichman, D. R.; Muller, D. A.; Hone, J. C. Grains and grain boundaries in highly crystalline monolayer molybdenum disulphide. *Nat. Mater.* **2013**, *12*, 554−561.
(12) He, Y.; Tang, P.; Hu, Z.; He, Q.; Zhu, C.; Wang, L.; Zeng, Q.; Golani, P.; Gao, G.; Fu, W.; Huang, Z.; Gao, C.; Xia, J.; Wang, X.; Wang, X.; Zhu, C.; Ramasse, Q. M.; Zhang, A.; An, B.; Zhang, Y.; Martí-Sánchez, S.; Morante, J. R.; Wang, L.; Tay, B. K.; Yakobson, B. I.; Trampert, A.; Zhang, H.; Wu, M.; Wang, Q. J.; Arbiol, J.; Liu, Z. Engineering grain boundaries at the 2D limit for the hydrogen evolution reaction. *Nat. Commun.* **2020**, *11*, 57.
(13) Zou, X.; Liu, Y.; Yakobson, B. I. Predicting dislocations and grain boundaries in two-dimensional metal-disulfides from the first principles. *Nano Lett.* **2013**, *13*, 253−258.
(14) Zhou, W.; Zou, X.; Najmaei, S.; Liu, Z.; Shi, Y.; Kong, J.; Lou, J.; Ajayan, P. M.; Yakobson, B. I.; Idrobo, J. C. Intrinsic structural defects in monolayer molybdenum disulfide. *Nano Lett.* **2013**, *13*, 2615−2622.
(15) Yu, Z. G.; Zhang, Y. W.; Yakobson, B. I. An anomalous formation pathway for dislocation-sulfur vacancy complexes in polycrystalline monolayer MoS_2. *Nano Lett.* **2015**, *15*, 6855−6861.
(16) Kang, K.; Xie, S.; Huang, L.; Han, Y.; Huang, P. Y.; Mak, K. F.; Kim, C. J.; Muller, D.; Park, J. High-mobility three-atom-thick semiconducting films with wafer-scale homogeneity. *Nature* **2015**, *520*, 656−660.
(17) Zhao, X.; Song, P.; Wang, C.; Riis-Jensen, A. C.; Fu, W.; Deng, Y.; Wan, D.; Kang, L.; Ning, S.; Dan, J.; Venkatesan, T.; Liu, Z.; Zhou, W.; Thygesen, K. S.; Luo, X.; Pennycook, S. J.; Loh, K. P. Engineering covalently bonded 2D layered materials by self-intercalation. *Nature* **2020**, *581*, 171−177.
(18) Cain, J. D.; Shi, F.; Wu, J.; Dravid, V. P. Growth mechanism of transition metal dichalcogenide monolayers: the role of self-seeding fullerene nuclei. *ACS Nano* **2016**, *10*, 5440−5445.
(19) Zhou, H.; Wang, C.; Shaw, J. C.; Cheng, R.; Chen, Y.; Huang, X.; Liu, Y.; Weiss, N. O.; Lin, Z.; Huang, Y.; Duan, X. Large area growth and electrical properties of p-type WSe_2 atomic layers. *Nano Lett.* **2015**, *15*, 709−713.
(20) Cheng, J.; Jiang, T.; Ji, Q.; Zhang, Y.; Li, Z.; Shan, Y.; Zhang, Y.; Gong, X.; Liu, W.; Wu, S. Kinetic nature of grain boundary formation in as-grown MoS_2 monolayers. *Adv. Mater.* **2015**, *27*, 4069−4074.
(21) Chen, S.; Gao, J.; Srinivasan, B. M.; Zhang, G.; Yang, M.; Chai, J.; Wang, S.; Chi, D.; Zhang, Y. W. Revealing the grain boundary formation mechanism and kinetics during polycrystalline MoS_2 growth. *ACS Appl. Mater. Interfaces* **2019**, *11*, 46090−46100.
(22) Zou, X.; Liu, M.; Shi, Z.; Yakobson, B. I. Environment-controlled dislocation migration and superplasticity in monolayer MoS_2. *Nano Lett.* **2015**, *15*, 3495−3500.
(23) Chen, J.; Wang, Y.; Xu, W.; Wen, Y.; Ryu, G. H.; Grossman, J. C.; Warner, J. H. Atomic structure of dislocations and grain boundaries in two-dimensional $PtSe_2$. *ACS Nano* **2021**, *15*, 16748−16759.
(24) Gnanasekaran, T.; Mahendran, K. H.; Kutty, K. V. G.; Mathews, C. K. Phase diagram studies on the Na-Mo-O system. *J. Nucl. Mater.* **1989**, *165*, 210−216.
(25) Li, S.; Lin, Y. C.; Zhao, W.; Wu, J.; Wang, Z.; Hu, Z.; Shen, Y.; Tang, D. M.; Wang, J.; Zhang, Q.; Zhu, H.; Chu, L.; Zhao, W.; Liu, C.; Sun, Z.; Taniguchi, T.; Osada, M.; Chen, W.; Xu, Q. H.; Wee, A. T. S.; Suenaga, K.; Ding, F.; Eda, G. Vapour-liquid-solid growth of monolayer MoS_2 nanoribbons. *Nat. Mater.* **2018**, *17*, 535−542.
(26) Yang, P.; Zou, X.; Zhang, Z.; Hong, M.; Shi, J.; Chen, S.; Shu, J.; Zhao, L.; Jiang, S.; Zhou, X.; Huan, Y.; Xie, C.; Gao, P.; Chen, Q.; Zhang, Q.; Liu, Z.; Zhang, Y. Batch production of 6-in. uniform monolayer molybdenum disulfide catalyzed by sodium in glass. *Nat. Commun.* **2018**, *9*, 979.
(27) Choi, M.-Y.; Choi, C.-W.; Yang, S.-J.; Lee, H.; Choi, S.; Park, J.-H.; Heo, J.; Choi, S.-Y.; Kim, C.-J. Substrate-dependent growth mode control of MoS_2 monolayers: implications for hydrogen evolution and field-effect transistors. *ACS Appl. Nano Mater.* **2022**, *5*, 4336−4342.
(28) Upmanyu, M.; Smith, R. W.; Srolovitz, D. J. Atomistic simulation of curvature driven grain boundary migration. *Interface Sci.* **1998**, *6*, 41−58.
(29) Hull, D.; Bacon, D. J. *Introduction to dislocations*; Butterworth-Heinemann: 2001.
(30) Lin, Y. C.; Dumcenco, D. O.; Huang, Y. S.; Suenaga, K. Atomic mechanism of the semiconducting-to-metallic phase transition in single-layered MoS_2. *Nat. Nanotechnol.* **2014**, *9*, 391−396.
(31) Huang, Q.; Zhu, Q.; Chen, Y.; Gong, M.; Li, J.; Zhang, Z.; Yang, W.; Wang, J.; Zhou, H.; Wang, J. Twinning-assisted dynamic adjustment of grain boundary mobility. *Nat. Commun.* **2021**, *12*, 6695.

https://doi.org/10.1021/acs.nanolett.3c00935
Nano Lett. XXXX, XXX, XXX−XXX

(32) Li, D.; Ding, F. Environment-Dependent Edge Reconstruction of Transition Metal Dichalcogenides: A Global Search. *Mater. Today Adv.* **2020**, *8*, 100079.
(33) Lien, D.-H.; Uddin, S. Z.; Yeh, M.; Amani, M.; Kim, H.; Ager, J. W., 3rd; Yablonovitch, E.; Javey, A. Electrical suppression of all nonradiative recombination pathways in monolayer semiconductors. *Science* **2019**, *364*, 468−471.
(34) Amani, M.; Lien, D.-H.; Kiriya, D.; Xiao, J.; Azcatl, A.; Noh, J.; Madhvapathy, S. R.; Addou, R.; KC, S.; Dubey, M.; Cho, K.; Wallace, R. M.; Lee, S.-C.; He, J.-H.; Ager, J. W.; Zhang, X.; Yablonovitch, E.; Javey, A. Near-unity photoluminescence quantum yield in MoS_2. *Science* **2015**, *350*, 1065−1068.
(35) Liang, T.; Habib, M. R.; Xiao, H.; Xie, S.; Kong, Y.; Yu, C.; Iwai, H.; Fujita, D.; Hanagata, N.; Chen, H.; Feng, Z.; Xu, M. Intrinsically substitutional carbon doping in CVD-grown monolayer MoS_2 and the band structure modulation. *ACS Appl. Electron. Mater.* **2020**, *2*, 1055−1064.
(36) Wang, Y.; Mao, J.; Meng, X.; Yu, L.; Deng, D.; Bao, X. Catalysis with two-dimensional materials confining single atoms: concept, design, and applications. *Chem. Rev.* **2019**, *119*, 1806−1854.
(37) Li, N.; Wang, Q.; Shen, C.; Wei, Z.; Yu, H.; Zhao, J.; Lu, X.; Wang, G.; He, C.; Xie, L.; Zhu, J.; Du, L.; Yang, R.; Shi, D.; Zhang, G. Large-scale flexible and transparent electronics based on monolayer molybdenum disulfide field-effect transistors. *Nat. Electron.* **2020**, *3*, 711−717.

https://doi.org/10.1021/acs.nanolett.3c00935
Nano Lett. XXXX, XXX, XXX−XXX